Chemical Science

ROYAL SOCIETY OF CHEMISTRY

EDGE ARTICLE

View Article Online
View Journal | View Issue

Cite this: *Chem. Sci.*, 2025, **16**, 23095

All publication charges for this article have been paid for by the Royal Society of Chemistry

Received 14th August 2025
Accepted 22nd October 2025

DOI: 10.1039/d5sc06200d

rsc.li/chemical-science

Exciplex spin-flip acceleration enables high-performance narrowband electroluminescence

Mengcheng Wang,†[a] Zhanxiang Chen,†*[a] Manli Huang,[b] Dengke Wang,[c] Cheng Zhong,[d] Zheng-Hong Lu[ce] and Chuluo Yang*[a]

Exciplex-forming systems that harvest triplet excitons *via* a triplet-to-singlet spin flip (reverse intersystem crossing, RISC) enable thermally activated delayed fluorescence, providing a route to boost light emission in organic light-emitting diodes. Here, we report heavy-atom-incorporated exciplexes in which the triplet state is predominantly localized on the heavy-atom fragment, resulting in large spin–orbit coupling. Through positional isomer optimization, the RISC rate constant reaches 4.9×10^6 s^{-1}, approximately an order of magnitude higher than in typical exciplexes. Organic light-emitting diodes based on the optimized exciplex host achieve a maximum external quantum efficiency (EQE) exceeding 40% and exhibit low efficiency roll-off (EQE > 33% at 1000 cd m^{-2}).

Introduction

The spin-triplet excitons are key determinants of efficiency and stability in organic optoelectronic devices.[1–4] For organic emitters, their triplet excitons are primarily harnessed by two pathways: phosphorescence through radiative triplet decay,[5–7] or thermally activated delayed fluorescence (TADF) *via* reverse intersystem crossing (RISC) from spin-forbidden triplets to spin-allowed singlets.[8–10] Recent developments have shown that TADF can be realized in materials featuring twisted donor (D)–acceptor (A) configurations,[11–15] or multiple-resonance (MR) nitrogen-boron fused polycyclic frameworks.[16–20] In both cases, the electron densities of the highest occupied and lowest unoccupied molecular orbitals (HOMO and LUMO) can be spatially separated by precise molecular design, thereby facilitating spin-flip of triplet excitons for efficient utilization.[21,22]

Another class of TADF materials, known as exciplexes, is formed in donor/acceptor (D/A) blends and offers greater design flexibility, attracting considerable industrial interest.[23,24] Upon photo- or electrical excitation, D and A form an excited-state complex in which the HOMO resides mainly on D and the LUMO on A, enabling through-space charge transfer and triplet-to-singlet spin flip.[25,26] In such exciplex systems, however, the lowest singlet (S_1) and triplet (T_1) states typically have dominant charge-transfer (CT) character, resulting in weak spin–orbit coupling (SOC) and consequently slow RISC;[27,28] reported exciplex TADF systems usually exhibit RISC rates (k_{RISC}) below 10^6 s^{-1}.[29–32] Slow RISC prolongs triplet lifetimes and promotes bimolecular exciton annihilation events, leading to severe efficiency roll-off in exciplex-based OLEDs.[33]

In this context, we are driven to accelerate the triplet-to-singlet spin flip in exciplex systems, achieving k_{RISC} of approximately 4.9×10^6 s^{-1}, about an order of magnitude higher than those typically other reported exciplexes. This RISC enhancement enables excellent performance in exciplex-based OLEDs, particularly at high brightness, surpassing state-of-the-art TADF, phosphorescent, TADF-sensitized hyperfluorescent and phosphorescence-sensitized hyperfluorescent OLEDs based on exciplex-forming co-hosts. Theoretical calculations and photophysical studies confirm that forming localized triplet states on heavy-atom-containing fragments, together with inducing additional orbital angular momentum through positional isomer optimization, drives the enhanced k_{RISC}, so as to reduce the triplet exciton concentration and minimize triplet-involved annihilations in the emission layer, and ultimately overcome the efficiency roll-off.

Results and discussion

Given that exciplex-forming co-hosts are based on bimolecular donor–acceptor systems,[27,34] and recognizing the relatively high electronegativity of selenium,[35–37] we strategically incorporated a planar five-membered selenium-containing heterocycle (dibenzo[*b*,*d*]selenophene) into the donor moiety. To minimize the

[a]*Shenzhen Key Laboratory of New Display and Storage Materials, College of Materials Science and Engineering, Shenzhen University, Shenzhen 518060, P. R. China. E-mail: zxchen@szu.edu.cn; clyang@whu.edu.cn*

[b]*Institute of Technology for Future Industry, School of Science and Technology Instrument Application Engineering, Shenzhen Institute of Information Technology, Shenzhen 518172, P. R. China*

[c]*Department of Physics, Center for Optoelectronics Engineering Research, Yunnan University, Kunming 650500, P. R. China*

[d]*Hubei Key Lab on Organic and Polymeric Optoelectronic Materials, Department of Chemistry, Wuhan University, Wuhan, 430072, P. R. China*

[e]*Department of Materials Science and Engineering, University of Toronto, Toronto, ON M5S 3E4, Canada*

† These authors contributed equally.

formation of labile bonds,[38] we specifically compared *meta*- and *para*-conjugation linkages (***m*SeCzCzCz** *vs.* ***p*SeCzCzCz**, Fig. 1a) for integrating selenium atom within the electron-donating framework. Density functional theory calculations (Fig. S1) indicated that ***m*SeCzCzCz** and ***p*SeCzCzCz** have similar dihedral angles between the dibenzo[*b*,*d*]selenophene and bicarbazole moieties (55.1° for ***m*SeCzCzCz** and 56.1° for ***p*SeCzCzCz**).

The selenium-containing donors (***m*SeCzCzCz** and ***p*SeCzCzCz**) were synthesized *via* a multi-step procedure (Scheme S1). The synthetic route commenced with a lithium–halogen exchange reaction, followed by hydrolysis to yield aromatic boric acids. Chlorinated dibenzo[*b*,*d*]selenophenes, serving as key intermediates, were prepared by trimethylsilyl cyanide-catalyzed intramolecular cyclization. The final products were obtained through the Buchwald–Hartwig coupling reaction. The chemical structures were fully characterized by ^{1}H NMR, ^{13}C NMR, and high-resolution mass spectrometry (Fig. S2–S11). Furthermore, the single-crystal structure of ***m*SeCzCzCz** (Fig. S12) revealed a twisted geometry between the peripheral dibenzo[*b*,*d*]selenophene group and the bicarbazole core. Notably, the crystal architecture displayed no significant π–π interactions. However, intermolecular C–H···Se interactions between the phenyl rings of bicarbazole and a neighboring molecule's selenium atom, along with multiple C–H···π interactions between neighboring dibenzo[*b*,*d*]selenophene and carbazole rings, were observed. Additionally, thermogravimetric analysis (Fig. S13) demonstrated their excellent thermal stability, with high decomposition temperatures (5% weight loss) of 420 °C and 408 °C for ***m*SeCzCzCz** and ***p*SeCzCzCz**, respectively, making them suitable for forming uniform films by thermal evaporation.

To construct blue-light-emitting exciplex systems, **SiTrzCz2** (9,9′-(6-(3-(triphenylsilyl)phenyl)-1,3,5-triazine-2,4-diyl)bis(9*H*-carbazole)) with high triplet energy (T_1 = 2.89 eV) was selected as an electron-withdrawing component and blended with selenium-containing donors of ***m*SeCzCzCz** and ***p*SeCzCzCz**, respectively (Fig. 1a). The steady-state photophysical properties of ***m*SeCzCzCz**, ***p*SeCzCzCz**, **SiTrzCz2**, and their 1 : 1 molar blends (***m*SeCzCz:SiTrzCz2** and ***p*SeCzCz:SiTrzCz2**, abbreviated as ***m*Se-EX** and ***p*Se-EX**) were investigated in solid films. As shown in Fig. 1b and c, both ***m*SeCzCzCz** and ***p*SeCzCzCz** exhibited absorption bands below 350 nm, closely matching the absorption of the reference molecule SiCzCz (9-(3-(triphenylsilyl)phenyl)-9*H*-3,9′-bicarbazole). The photoluminescence (PL) spectra of ***m*SeCzCzCz** and ***p*SeCzCzCz** films displayed emission maxima at 386 nm and 406 nm, respectively, with the latter showing a distinct red shift relative to **SiCzCz**. Interestingly, their 1 : 1 molar blends with **SiTrzCz2** (***m*Se-EX** and ***p*Se-EX**) exhibited identical broad emission bands centered at 467 nm, slightly blue-shifted compared to the control exciplex (**SiCzCz:SiTrzCz2**, termed **Si-EX**). Phosphorescence spectra measured at 77 K (Fig. S14) revealed T_1 energies of 2.77 eV for ***m*SeCzCzCz** and 2.84 eV for ***p*SeCzCzCz**,

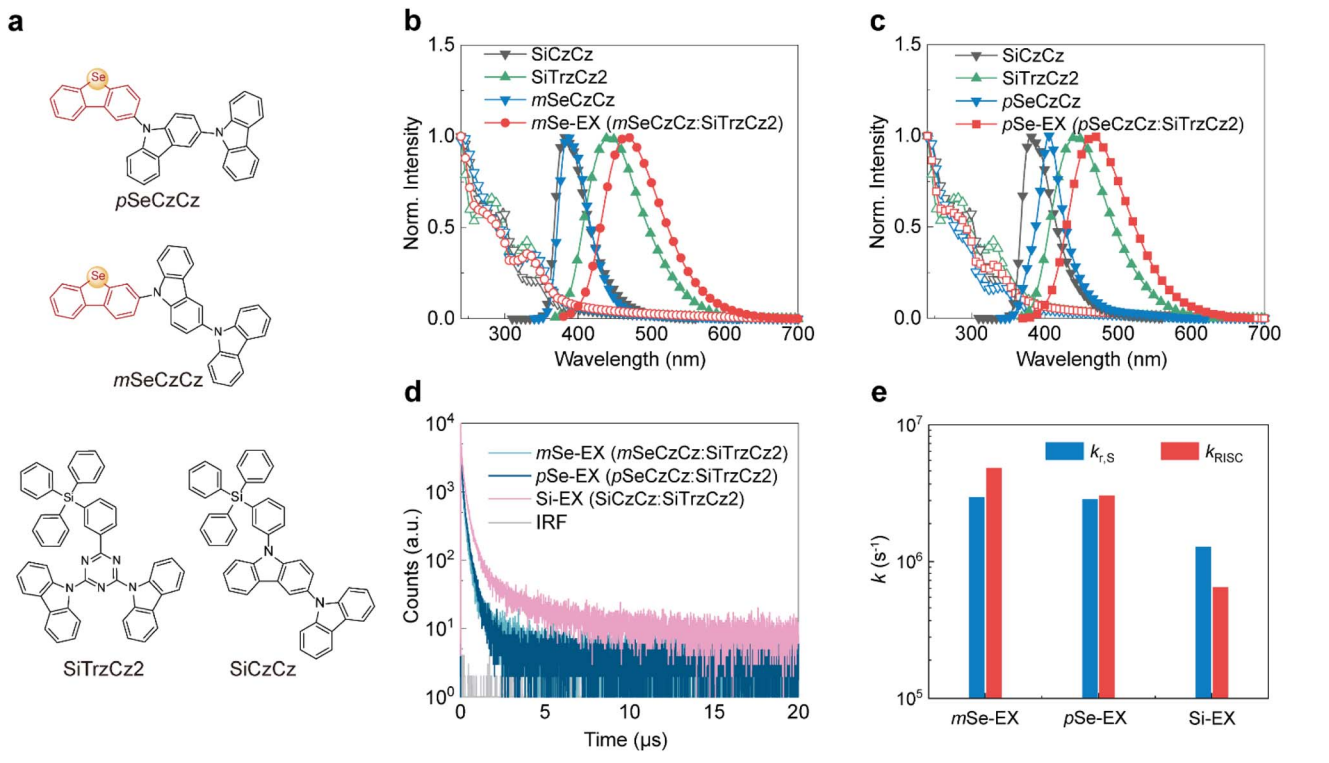

Fig. 1 (a) Chemical structures of the compounds. (b) Normalized UV-visible absorption spectra (open symbols) and PL spectra (filled symbols) of **SiCzCz**, **SiTrzCz2**, ***m*SeCzCzCz** and their exciplex blend ***m*SeCzCz:SiTrzCz2** (***m*Se-EX**). (c) Normalized UV-visible absorption spectra (open symbols) and PL spectra (filled symbols) of **SiCzCz**, **SiTrzCz2**, ***p*SeCzCzCz** and their exciplex blend ***p*SeCzCz:SiTrzCz2** (***p*Se-EX**). (d) Transient PL decay curves of ***m*Se-EX**, ***p*Se-EX** and the reference exciplex **SiCzCz:SiTrzCz2** (**Si-EX**) films under excitation at 375 nm. (e) Comparison of calculated rate constants for singlet radiative decay ($k_{r,S}$) and reverse intersystem crossing (k_{RISC}).

determined from the onsets of these spectra. The broad phosphorescence emission band around 500 nm arises from the cumulative contribution of multiple vibronic bands associated with LE-state emission. As anticipated, ***m*Se-EX** and ***p*Se-EX** films clearly exhibited prompt and delayed fluorescence components (Fig. 1d), confirming efficient RISC within these exciplexes. The corresponding prompt (τ_{PF}) and delayed (τ_{DF}) lifetimes of ***m*Se-EX** (58.5 ns/0.3 μs) and ***p*Se-EX** (72.0 ns/0.4 μs) were significantly shorter than those of **Si-EX** (186.8 ns/1.9 μs), despite similar PL quantum yields (31%, 29%, and 30% for ***m*Se-EX**, ***p*Se-EX**, and **Si-EX**, respectively). Key kinetic constants, including singlet radiative decay rate ($k_{r,S}$), singlet nonradiative decay rate ($k_{nr,S}$), intersystem crossing rate (k_{ISC}) and RISC rate (k_{RISC}), were extrapolated and are summarized in Fig. 1e and Table 1 (see SI for detailed calculation methods).[39,40] Notably, ***m*Se-EX** and ***p*Se-EX** showed significantly enhanced $k_{r,S}$ values (3.0×10^6 s^{-1} and 2.9×10^6 s^{-1}, respectively) relative to **Si-EX** (1.3×10^6 s^{-1}). Selenium incorporation also accelerated singlet nonradiative contributions, including $k_{nr,S}$ (5.4×10^6 s^{-1} for ***m*Se-EX**, 6.8×10^6 s^{-1} for ***p*Se-EX** and 2.9×10^6 s^{-1} for **Si-EX**) and k_{ISC} (6.1×10^6 s^{-1} for ***m*Se-EX**, 3.3×10^6 s^{-1} for ***p*Se-EX** and 1.0×10^6 s^{-1} for **Si-EX**), resulting in similar PL quantum yields across these exciplex systems. More importantly, ***m*Se-EX** and ***p*Se-EX** demonstrated substantially increased k_{RISC} values (4.9×10^6 s^{-1} and 3.1×10^6 s^{-1}, respectively) compared to **Si-EX** (6.9×10^5 s^{-1}), indicating that selenium integration in exciplex systems promotes faster consumption of triplet excitons. This trend is consistent with other selenium-containing TADF emitters, and the k_{RISC} values of ***m*Se-EX** and ***p*Se-EX** surpass those of most previously reported selenium-containing TADF molecules (typically in the order of 10^5–10^6 s^{-1}).[41–45]

To clarify the enhanced k_{RISC} in ***m*Se-EX** relative to ***p*Se-EX**, we performed time-dependent density functional theory calculations to analyse SOC matrix elements and natural transition orbital (NTO) distributions, with **Si-EX** as the reference. The SOC matrix elements for the $T_1 \rightarrow S_1$ transition (Fig. 2a) in ***m*Se-EX** (3.606 cm^{-1}) and ***p*Se-EX** (3.136 cm^{-1}) were markedly higher than that of **Si-EX** (0.265 cm^{-1}), corresponding to 13.6- and 11.8-fold enhancements, respectively (Fig. 2b). NTO analysis indicated charge-transfer characteristics in the S_1 states of all exciplexes (Fig. S15), while their T_1 states exhibited localized excitations (Fig. 2c). In **Si-EX**, the T_1 state primarily localized on the benzene unit of tetraphenylsilane and the *meta*-connected

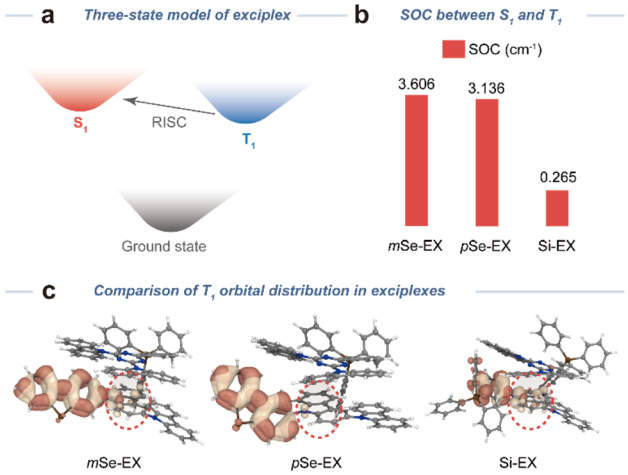

Fig. 2 (a) Schematic illustration of potential energy surfaces for the ground state (black), the lowest singlet state (S_1, red), and the lowest triplet state (T_1, blue) within the exciplex. (b) Comparison of calculated spin–orbit coupling (SOC) values between the S_1 and T_1 states for *m*Se-EX, *p*Se-EX, and Si-EX systems. (c) Hole–electron distributions of T_1 orbitals for *m*Se-EX, *p*Se-EX, and Si-EX at their optimized T_1 geometries.

carbazole groups. Conversely, the T_1 state in ***p*Se-EX** was mainly localized on the dibenzo[*b*,*d*]selenophene fragment, and the selenium incorporation enhanced the SOC between T_1 and S_1 states. Notably, for ***m*Se-EX**, the T_1 state extended from the dibenzo[*b*,*d*]selenophene fragment to the *meta*-connected carbazole group *via* two-lobed p-orbitals. The rotational overlap of adjacent p-orbitals generated additional orbital angular momentum, amplifying SOC and thereby enhancing k_{RISC} in ***m*Se-EX**.[46]

To further investigate the exciplex hosts with fast k_{RISC} on MR-TADF emitters, we incorporated *ν*-DABNA as the emitter into ***m*Se-EX**, ***p*Se-EX**, and **Si-EX** host matrices. PL spectra of the doped films (Fig. S16) showed a narrow emission peak at 470 nm with a FWHM of 17 nm, confirming efficient Förster resonance energy transfer (FRET) from the exciplex host to the MR-TADF emitter. Time-resolved emission spectra (Fig. 3a–c) revealed shorter delayed fluorescence lifetimes for ***m*Se-EX:*ν*-DABNA** (2.8 μs) and ***p*Se-EX:*ν*-DABNA** (3.0 μs) compared to **Si-EX:*ν*-DABNA** (4.0 μs). Additionally, the delayed component

Table 1 Photophysical properties of *m*SeCzCz:SiTrzCz2 (*m*Se-EX), *p*SeCzCz:SiTrzCz2 (*p*Se-EX) and the reference exciplex SiCzCz:SiTrzCz2 (Si-EX)

Film	λ_{PL}[a] [nm]	Φ_{PL}[b] [%]	τ_p[c] [ns]	τ_d[d] [μs]	$k_{r,S}$[e] [s^{-1}]	$k_{nr,S}$[f] [s^{-1}]	k_{ISC}[g] [s^{-1}]	k_{RISC}[h] [s^{-1}]
***m*Se-EX**	467	31	58.5	0.3	3.0×10^6	5.4×10^6	6.1×10^6	4.9×10^6
***p*Se-EX**	467	29	72.0	0.4	2.9×10^6	6.8×10^6	3.3×10^6	3.1×10^6
Si-EX	470	30	186.8	1.9	1.3×10^6	2.9×10^6	1.0×10^6	6.9×10^5

[a] Peak wavelength of the photoluminescence spectra in the film. [b] Absolute photoluminescence quantum yield measured with an integration-sphere system under an argon atmosphere. [c] Lifetime of the prompt component determined from the transient photoluminescence decay curve at 298 K. [d] Lifetime of the delayed component determined from the transient photoluminescence decay curve at 298 K. [e] Rate constant of singlet radiative decay. [f] Rate constant of singlet nonradiative decay. [g] Rate constant of intersystem crossing. [h] Rate constant of reverse intersystem crossing.

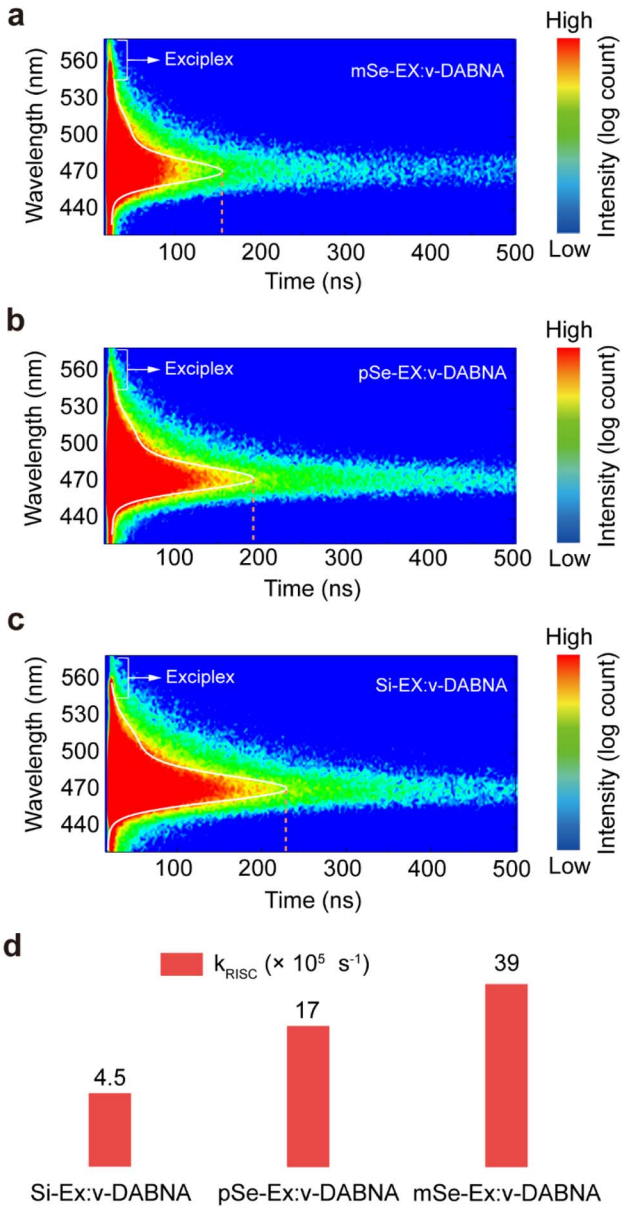

Fig. 3 (a)–(c) Time-dependent emission contour maps of (a) ***m*Se-EX:*v*-DABNA**, (b) ***p*Se-EX:*v*-DABNA**, and (c) **Si-EX:*v*-DABNA** films, recorded between 420 and 580 nm. (d) Comparison of calculated reverse intersystem crossing rate constants (k_{RISC}) of ***m*Se-EX:*v*-DABNA**, ***p*Se-EX:*v*-DABNA** and **Si-EX:*v*-DABNA** films.

contribution was highest for ***m*Se-EX:*v*-DABNA** (91%), followed by ***p*Se-EX:*v*-DABNA** (80%) and **Si-EX:*v*-DABNA** (45%). All doped films exhibited near-unity PL quantum yields of 99% (***m*Se-EX:*v*-DABNA**), 97% (***p*Se-EX:*v*-DABNA**), and 99% (**Si-EX:*v*-DABNA**). Consequently, the calculated k_{RISC} values (Fig. 3d) were progressively increased from 4.5×10^5 s^{-1} (**Si-EX:*v*-DABNA**) to 1.7×10^6 s^{-1} (***p*Se-EX:*v*-DABNA**) and 3.9×10^6 s^{-1} (***m*Se-EX:*v*-DABNA**). These results align closely with theoretical predictions, clearly demonstrating that exciplex hosts with fast k_{RISC} substantially accelerate the RISC process in MR-TADF emitters.

Encouraged by the near-unity PL quantum yield and accelerated RISC process of *v*-DABNA in the selenium-based exciplex hosts, we fabricated corresponding OLED devices with the following architecture: indium tin oxide (50 nm)/1,4,5,8,9,11-hexaazatriphenylenehexacarbonitrile (HATCN, 5 nm)/4,4′-cyclohexylidenebis[*N*,*N*-bis(4-methylphenyl) benzenamine] (TAPC, 30 nm)/tris(4-carbazoyl-9-ylphenyl) amine (TCTA, 15 nm)/Se donor (15 nm)/Se donor:**SiTrzCz2:*v*-DABNA** (35 nm, 49.5 wt%:49.5 wt%:1 wt%)/SiTrzCz2 (15 nm)/1-(4-(10-([1,1′-biphenyl]-4-yl)anthracen-9-yl)phenyl)-2-ethyl-1*H*-benzo[*d*]-imidazole (ANT-BIZ, 30 nm)/lithium quinolin-8-olate (Liq, 2 nm)/aluminium (Al, 100 nm). Specifically, for the emitting layers, *v*-DABNA was co-evaporated with the ***m*Se-EX** (***m*SeCzCz:SiTrzCz2**) host for device A, and the ***p*Se-EX** (***p*SeCzCz:SiTrzCz2**) host for device B. For comparison, a control device based on the **Si-EX** (**SiCzCz:SiTrzCz2**) host was also prepared. In this device architecture, HATCN, TAPC and TCTA served as hole-injection and hole-transport layers, while ANT-BIZ and Liq functioned as the electron-transport and electron-injection layers, respectively. Additionally, Se-containing donors (***m*SeCzCz** or ***p*SeCzCz**) and **SiTrzCz2** acted as electron-blocking and hole-blocking layers, respectively. The device structure and corresponding energy level diagram are illustrated in Fig. 4a and b, and chemical structures of the organic materials are provided in Fig. S17. The electroluminescence properties are summarized in Table 2.

All fabricated devices exhibited nearly identical blue emission profiles (Fig. S18) peaking at 470 nm, with a narrow FWHM of 17 nm, closely matching the corresponding PL spectra obtained from thin films. This indicates complete FRET from the exciplex hosts to the *v*-DABNA emitter. According to the current density–voltage–luminance (*J*–*V*–*L*) curves (Fig. 4c), device A exhibited a turn-on voltage of approximately 3.2 V, an operating voltage of 4.2 V at a luminance of 1000 cd m^{-2}, and a maximum luminance of 36 603 cd m^{-2}. In comparison, device B showed a higher turn-on voltage of approximately 3.6 V, an operating voltage of 5.0 V at 1000 cd m^{-2}, and a lower maximum luminance of 33 204 cd m^{-2}. The EL spectra remained stable under high-brightness (~10 000 cd m^{-2}) or high-voltage (~8 V) for all devices, indicating that the exciton recombination zone was essentially unchanged under these operating conditions (Fig. S19). Device A also achieved higher maximum current efficiency (39.7 cd A^{-1}) and power efficiency (39.0 lm W^{-1}) compared with device B, which displayed maximum current and power efficiencies of 31.1 cd A^{-1} and 27.1 lm W^{-1}, respectively (Fig. 4d).

As shown in Fig. 4e, device A achieved a maximum EQE of 40.9% (average: 40.45 ± 0.29%, based on the measurements of 11 independent devices; Fig. S20), substantially exceeding those of device B (33.7%) and the control device (34.1%). This exceptional performance stemmed from the near-unity PL quantum yield of the emissive layer and favorable horizontal orientation of the transition dipole moment of *v*-DABNA doped in the ***m*Se-EX** host (transition dipole moment vector $S = -0.46$, Fig. S21).[47] Compared to the control device, devices A and B demonstrated significantly reduced efficiency roll-off, resulting from enhanced SOC values between the singlet and triplet manifolds provided by the ***m*Se-EX** and ***p*Se-EX**

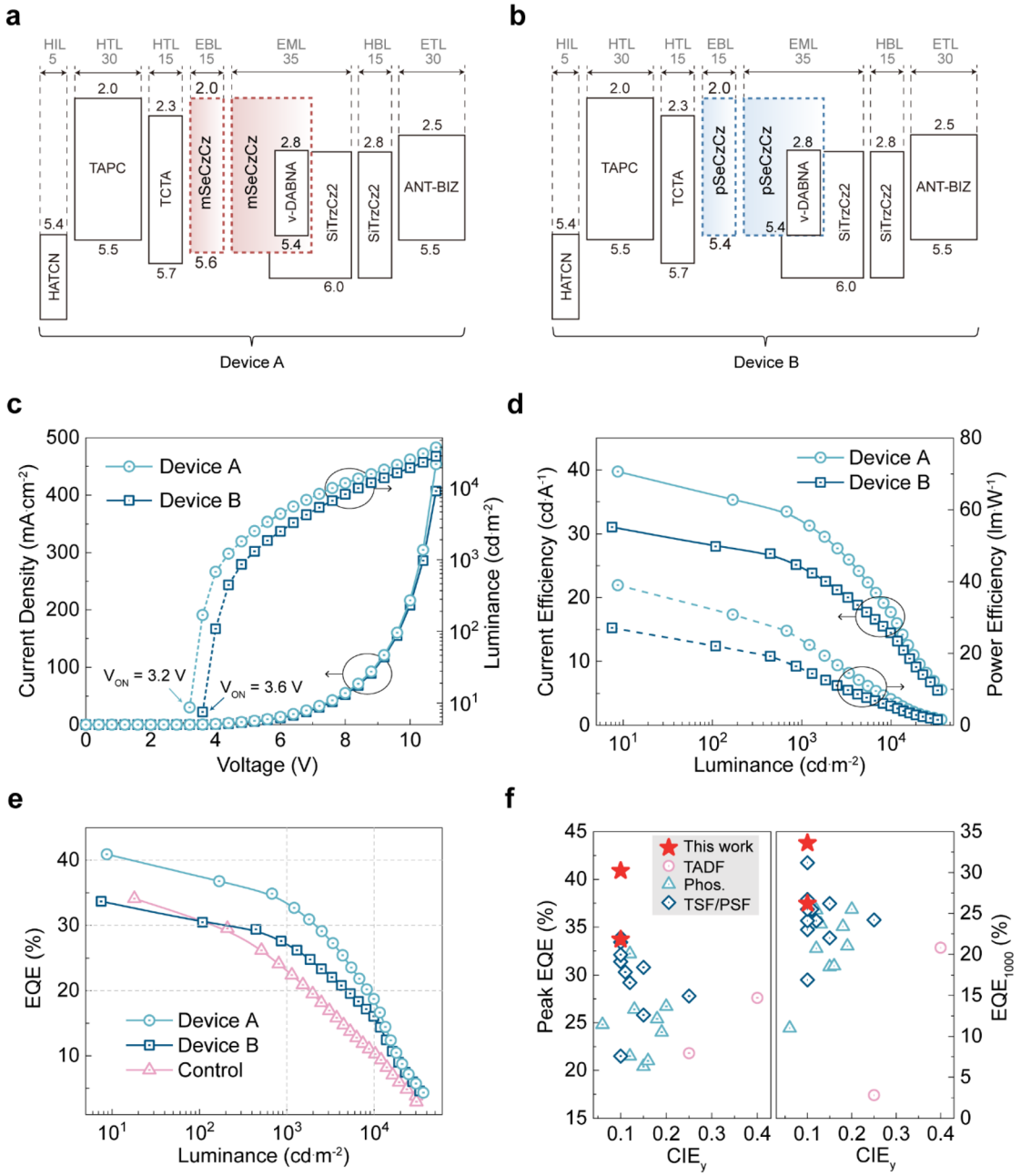

Fig. 4 (a) and (b) Device architecture and energy-level diagram of OLEDs based on (a) *m*SeCzCz:SiTrzCz2:*v*-DABNA (device A) and (b) *p*SeCzCz:SiTrzCz2:*v*-DABNA (device B). (c) Current density and luminance *versus* voltage (*J*–*V*–*L*) characteristics, and (d) current and power efficiency *versus* luminance curves for device A and device B. (e) External quantum efficiency (EQE) *versus* luminance plots of device A, device B and the control device. (f) Peak EQE and EQE at 1000 cd m^{-2} (EQE_{1000}) plotted against the Commission Internationale de l'Eclairage y-coordinate (CIE_y) for representative blue OLEDs employing exciplex-forming co-hosts. Definitions and references for these OLEDs are summarized in Table S1. TSF, TADF-sensitized fluorescence; PSF, phosphorescence-sensitized fluorescence.

hosts, which effectively suppresses triplet-involved annihilation processes at high brightness levels. Notably, owing to the stronger SOC provided by the ***m*Se-EX** host, device A exhibited considerably lower efficiency roll-off compared to recent blue OLEDs utilizing exciplex-forming co-host systems. Remarkably, device A maintained an EQE of 33.6% at a practical luminance of 1000 cd m^{-2}, surpassing those of state-of-the-art TADF, phosphorescent, TADF-sensitized hyperfluorescent and phosphorescence-sensitized hyperfluorescent OLEDs based on exciplex-forming co-hosts (Fig. 4f and Table S1). These results clearly demonstrate that the exciplex hosts with fast RISC can effectively accelerate the RISC process in MR-TADF emitters, thereby substantially enhancing device performance under realistic display operating conditions.

Table 2 Summary performance of the devices

			EQE[c] [%]			CE[d] [cd A^{-1}]		PE[e] [lm W^{-1}]			
Device	λ_{PL}[a] [nm]	L_{max}[b] [cd m^{-2}]	Max	1000 cd m^{-2}	Roll-off	Max	1000 cd m^{-2}	Max	1000 cd m^{-2}	FWHM[f] [nm]	CIE(x,y)[g]
Device A	470	36 603	40.9	33.6	17.8	39.7	32.2	39.0	23.9	17	(0.13, 0.12)
Device B	470	33 204	33.7	26.2	22.3	31.1	23.9	27.1	14.4	17	(0.12, 0.12)
Control	470	30 511	34.1	22.4	34.3	35.8	23.1	40.2	16.5	17	(0.13, 0.12)

[a] Electroluminescence peak wavelength recorded at 1000 cd m^{-2}. [b] Maximum luminance. [c] Maximum external quantum efficiency, and value at 1000 cd m^{-2}. [d] Maximum current efficiency, and value at 1000 cd m^{-2}. [e] Maximum power efficiency, and value at 1000 cd m^{-2}. [f] Full width at half-maximum. [g] CIE coordinates.

Conclusions

In summary, we have developed a heavy-atom-incorporated exciplex with k_{RISC} as far as 4.9×10^6 s^{-1}, an order of magnitude higher than the typical values for exciplexes. The heavy atom participates directly in the triplet-state orbital distribution, resulting in strong spin–orbit coupling; combined with positional isomer optimization, this accelerates the spin-flip process. Notably, employing this exciplex with fast RISC as a host also enhances the k_{RISC} of the MR-TADF emitter to the 10^6 s^{-1} range. Devices employing the selenium-containing ***m*Se-EX** host exhibited exceptional electroluminescence performance, achieving a high EQE_{max} of 40.9% and minimal efficiency roll-off (EQE = 33.6% at 1000 cd m^{-2}). We believe that the simple design and in-depth structure–property relationship established here would aid in the development of exciplex systems with efficient spin-flip transition and benefit the electroluminescence efficiency in narrowband OLEDs.

Author contributions

Z. Chen and C. Yang conceived and supervised the project. M. Wang synthesized and characterized the hosts, and performed photophysical measurements under the supervision of Z. Chen. Z. Chen and M. Huang fabricated the OLEDs and characterized the performance of the devices. Z. Chen performed theoretical calculations. D. Wang and Z.-H. Lu contributed to the UPS results. Z. Chen, M. Huang, C. Zhong, and C. Yang participated in discussions. All authors engaged in result analysis and provided feedback on the manuscript.

Conflicts of interest

There are no conflicts of interest to declare.

Data availability

The data supporting this article have been included as part of the SI. Supplementary information: all synthetic procedures, characterization data, spectroscopic data, supplementary figures and tables, and detailed information. See DOI: **https://doi.org/10.1039/d5sc06200d**.

CCDC 2408523 (***m*SeCzCz**) contains the supplementary crystallographic data for this paper.[48]

Acknowledgements

We acknowledge financial support from the National Natural Science Foundation of China (52130308 and 52403237), GuangDong Basic and Applied Basic Research Foundation (2022A1515110445), the Shenzhen Technology and Innovation Commission (RCBS20231211090518026, ZDSYS20210623091813040), Research Team Cultivation Program of Shenzhen University (2023DFT004), and Scientific Foundation for Youth Scholars of Shenzhen University (868-000001033371). We also thank the Instrumental Analysis Center of Shenzhen University for the analytical support.

References

1 Z. Tang, F. Lyu, J. Gu, H. Guo, W. Yu, Y. Zou, L. Gong, R. Tang, B. Qu, X. Guo, Y. Chen, Y. Deng, M. Bian, Y. Li, D. Zhang, M. Wei, S. M. Park, P. Xia, Y. Lv, Q. Gong, S. Wang, Z. Chen and L. Xiao, Sub-Second Long Lifetime Triplet Exciton Reservoir for Highly Efficient and Stable Organic Light-Emitting Diode, *Adv. Mater.*, 2024, **36**, 2313746.

2 Q. Meng, R. Wang, Y. Wang, X. Guo, Y. Liu, X. Wen, C. Yao and J. Qiao, Longevity gene responsible for robust blue organic materials employing thermally activated delayed fluorescence, *Nat. Commun.*, 2023, **14**, 3927.

3 Y. H. Jung, G. S. Lee, S. Murugananthan, H. R. Kim, J. H. Oh, J. H. Ham, S. B. Yadav, J. H. Lee, M. Y. Chae, Y. H. Kim and J. H. Kwon, Modified t-butyl in tetradentate platinum (II) complexes enables exceptional lifetime for blue-phosphorescent organic light-emitting diodes, *Nat. Commun.*, 2024, **15**, 2977.

4 H. H. Cho, D. G. Congrave, A. J. Gillett, S. Montanaro, H. E. Francis, V. Riesgo-Gonzalez, J. Ye, R. Chowdury, W. Zeng, M. K. Etherington, J. Royakkers, O. Millington, A. D. Bond, F. Plasser, J. M. Frost, C. P. Grey, A. Rao, R. H. Friend, N. C. Greenham and H. Bronstein, Suppression of Dexter transfer by covalent encapsulation for efficient matrix-free narrowband deep blue hyperfluorescent OLEDs, *Nat. Mater.*, 2024, **23**, 519–526.

5 H. Zhao, C. E. Arneson, D. Fan and S. R. Forrest, Stable blue phosphorescent organic LEDs that use polariton-enhanced Purcell effects, *Nature*, 2024, **626**, 300–305.

6 M. A. Baldo, D. F. O'Brien, Y. You, A. Shoustikov, S. Sibley, M. E. Thompson and S. R. Forrest, Highly efficient phosphorescent emission from organic electroluminescent devices, *Nature*, 1998, **395**, 151–154.
7 Y. Ma, H. Zhang, J. Shen and C. Che, Electroluminescence from triplet metal-ligand charge-transfer excited state of transition metal complexes, *Synth. Met.*, 1998, **94**, 245–248.
8 Z. Chen, F. Ni, Z. Wu, Y. Hou, C. Zhong, M. Huang, G. Xie, D. Ma and C. Yang, Enhancing Spin-Orbit Coupling by Introducing a Lone Pair Electron with p Orbital Character in a Thermally Activated Delayed Fluorescence Emitter: Photophysics and Devices, *J. Phys. Chem. Lett.*, 2019, **10**, 2669–2675.
9 Z. Chen, Z. Wu, F. Ni, C. Zhong, W. Zeng, D. Wei, K. An, D. Ma and C. Yang, Emitters with a pyridine-3,5-dicarbonitrile core and short delayed fluorescence lifetimes of about 1.5 μs: orange-red TADF-based OLEDs with very slow efficiency roll-offs at high luminance, *J. Mater. Chem. C*, 2018, **6**, 6543–6548.
10 H. Uoyama, K. Goushi, K. Shizu, H. Nomura and C. Adachi, Highly efficient organic light-emitting diodes from delayed fluorescence, *Nature*, 2012, **492**, 234–238.
11 T. Huang, Q. Wang, H. Zhang, Y. Xin, Y. Zhang, X. Chen, D. Zhang and L. Duan, Delocalizing electron distribution in thermally activated delayed fluorophors for high-efficiency and long-lifetime blue electroluminescence, *Nat. Mater.*, 2024, **23**, 1523–1530.
12 T. Huang, Q. Wang, H. Zhang, Y. Zhang, G. Zhan, D. Zhang and L. Duan, Enhancing the efficiency and stability of blue thermally activated delayed fluorescence emitters by perdeuteration, *Nat. Photonics*, 2024, **18**, 516–523.
13 Y. Wada, H. Nakagawa, S. Matsumoto, Y. Wakisaka and H. Kaji, Organic light emitters exhibiting very fast reverse intersystem crossing, *Nat. Photonics*, 2020, **14**, 643–649.
14 M. Y. Wong and E. Zysman-Colman, Purely Organic Thermally Activated Delayed Fluorescence Materials for Organic Light-Emitting Diodes, *Adv. Mater.*, 2017, **29**, 1605444.
15 S. Hirata, Y. Sakai, K. Masui, H. Tanaka, S. Y. Lee, H. Nomura, N. Nakamura, M. Yasumatsu, H. Nakanotani, Q. Zhang, K. Shizu, H. Miyazaki and C. Adachi, Highly efficient blue electroluminescence based on thermally activated delayed fluorescence, *Nat. Mater.*, 2015, **14**, 330–336.
16 T. Hua, X. Cao, J. Miao, X. Yin, Z. Chen, Z. Huang and C. Yang, Deep-blue organic light-emitting diodes for ultrahigh-definition displays, *Nat. Photonics*, 2024, **18**, 1161–1169.
17 T. Hatakeyama, K. Shiren, K. Nakajima, S. Nomura, S. Nakatsuka, K. Kinoshita, J. Ni, Y. Ono and T. Ikuta, Ultrapure Blue Thermally Activated Delayed Fluorescence Molecules: Efficient HOMO–LUMO Separation by the Multiple Resonance Effect, *Adv. Mater.*, 2016, **28**, 2777–2781.
18 M. Yang, I. S. Park and T. Yasuda, Full-Color, Narrowband, and High-Efficiency Electroluminescence from Boron and Carbazole Embedded Polycyclic Heteroaromatics, *J. Am. Chem. Soc.*, 2020, **142**, 19468–19472.
19 J. M. Dos Santos, D. Hall, B. Basumatary, M. Bryden, D. Chen, P. Choudhary, T. Comerford, E. Crovini, A. Danos, J. De, S. Diesing, M. Fatahi, M. Griffin, A. K. Gupta, H. Hafeez, L. Hämmerling, E. Hanover, J. Haug, T. Heil, D. Karthik, S. Kumar, O. Lee, H. Li, F. Lucas, C. F. R. Mackenzie, A. Mariko, T. Matulaitis, F. Millward, Y. Olivier, Q. Qi, I. D. W. Samuel, N. Sharma, C. Si, L. Spierling, P. Sudhakar, D. Sun, E. Tankelevičiūtė, M. Duarte Tonet, J. Wang, T. Wang, S. Wu, Y. Xu, L. Zhang and E. Zysman-Colman, The Golden Age of Thermally Activated Delayed Fluorescence Materials: Design and Exploitation, *Chem. Rev.*, 2024, **124**, 13736–14110.
20 X. Fan, K. Wang, Y. Shi, Y. Cheng, Y. Lee, J. Yu, X. Chen, C. Adachi and X. Zhang, Ultrapure green organic light-emitting diodes based on highly distorted fused π-conjugated molecular design, *Nat. Photonics*, 2023, **17**, 280–285.
21 T. Wu, M. Huang, C. Lin, P. Huang, T. Chou, R. Chen-Cheng, H. Lin, R. Liu and C. Cheng, Diboron compound-based organic light-emitting diodes with high efficiency and reduced efficiency roll-off, *Nat. Photonics*, 2018, **12**, 235–240.
22 X. Fan, X. Tang, T. Zhang, S. Kohata, J. Yu, X. Chen, K. Wang, T. Hatakeyama, C. Adachi and X. Zhang, Stable narrowband blue OLEDs by modulating frontier molecular orbital levels, *Nat. Commun.*, 2025, **16**, 4936.
23 H. Shin, J. H. Lee, C. K. Moon, J. S. Huh, B. Sim and J. J. Kim, Sky-Blue Phosphorescent OLEDs with 34.1% External Quantum Efficiency Using a Low Refractive Index Electron Transporting Layer, *Adv. Mater.*, 2016, **28**, 4920–4925.
24 H. G. Kim, K. H. Kim and J. J. Kim, Highly Efficient, Conventional, Fluorescent Organic Light-Emitting Diodes with Extended Lifetime, *Adv. Mater.*, 2017, **29**, 1702159.
25 C. K. Moon, K. Suzuki, K. Shizu, C. Adachi, H. Kaji and J. J. Kim, Combined Inter- and Intramolecular Charge-Transfer Processes for Highly Efficient Fluorescent Organic Light-Emitting Diodes with Reduced Triplet Exciton Quenching, *Adv. Mater.*, 2017, **29**, 1606448.
26 X. Tang, L. Cui, H. Li, A. J. Gillett, F. Auras, Y. Qu, C. Zhong, S. T. E. Jones, Z. Jiang, R. H. Friend and L.-S. Liao, Highly efficient luminescence from space-confined charge-transfer emitters, *Nat. Mater.*, 2020, **19**, 1332–1338.
27 C. K. Moon, J. S. Huh, J. M. Kim and J. J. Kim, Electronic Structure and Emission Process of Excited Charge Transfer States in Solids, *Chem. Mater.*, 2018, **30**, 5648–5654.
28 K. H. Kim, S. J. Yoo and J. J. Kim, Boosting Triplet Harvest by Reducing Nonradiative Transition of Exciplex toward Fluorescent Organic Light-Emitting Diodes with 100% Internal Quantum Efficiency, *Chem. Mater.*, 2016, **28**, 1936–1941.
29 K. Goushi, K. Yoshida, K. Sato and C. Adachi, Organic light-emitting diodes employing efficient reverse intersystem crossing for triplet-to-singlet state conversion, *Nat. Photonics*, 2012, **6**, 253–258.
30 Z. Chen, C. Zhong, J. Han, J. Miao, Y. Qi, Y. Zou, G. Xie, S. Gong and C. Yang, High-Performance Circularly Polarized Electroluminescence with Simultaneous

Narrowband Emission, High Efficiency, and Large Dissymmetry Factor, *Adv. Mater.*, 2022, **34**, 2109147.
31 J. Sun, H. Ahn, S. Kang, S. Ko, D. Song, H. A. Um, S. Kim, Y. Lee, P. Jeon, S. Hwang, Y. You, C. Chu and S. Kim, Exceptionally stable blue phosphorescent organic light-emitting diodes, *Nat. Photonics*, 2022, **16**, 212–218.
32 C. Duan, C. Han, J. Zhang, X. Zhang, C. Fan and H. Xu, Manipulating Charge-Transfer Excitons by Exciplex Matrix: Toward Thermally Activated Delayed Fluorescence Diodes with Power Efficiency beyond 110 lm W^{-1}, *Adv. Funct. Mater.*, 2021, **31**, 2102739.
33 S. Diesing, L. Zhang, E. Zysman-Colman and I. D. W. Samuel, A figure of merit for efficiency roll-off in TADF-based organic LEDs, *Nature*, 2024, **627**, 747–753.
34 H. A. Al Attar and A. P. Monkman, Electric Field Induce Blue Shift and Intensity Enhancement in 2D Exciplex Organic Light Emitting Diodes; Controlling Electron-Hole Separation, *Adv. Mater.*, 2016, **28**, 8014–8020.
35 G. L. Gibson, T. M. McCormick and D. S. Seferos, Atomistic Band Gap Engineering in Donor-Acceptor Polymers, *J. Am. Chem. Soc.*, 2012, **134**, 539–547.
36 Z. Chen, X. Li, J. Zhao, S. Zhang, J. Wang, H. Zhang, J. Zhang, Q. Dong, W. Zhang, W. Hu and X. Han, Stabilizing Pt Single Atoms through Pt-Se Electron Bridges on Vacancy-enriched Nickel Selenide for Efficient Electrocatalytic Hydrogen Evolution, *Angew. Chem., Int. Ed.*, 2023, **62**, e202308686.
37 W. Jiang, S. Wu, D. Xu, L. Tu, Y. Xie, P. Pasqués-Gramage, P. G. Boj, M. A. Díaz-García, F. Li, J. Wu and Z. Li, Stable Xanthene Radicals and Their Heavy Chalcogen Analogues Showing Tunable Doublet Emission from Green to Near-infrared, *Angew. Chem., Int. Ed.*, 2025, **64**, e202418762.
38 R. Wang, Y. Wang, N. Lin, R. Zhang, L. Duan and J. Qiao, Effects of Ortho-Linkages on the Molecular Stability of Organic Light-Emitting Diode Materials, *Chem. Mater.*, 2018, **30**, 8771–8781.
39 M. Huang, Z. Chen, J. Miao, S. He, W. Yang, Z. Huang, Y. Zou, S. Gong, Y. Tan and C. Yang, Harmonization of rapid triplet up-conversion and singlet radiation enables efficient and stable white OLEDs, *Nat. Commun.*, 2024, **15**, 8048.
40 Z. Chen, M. Huang, C. Zhong, X. Cao, G. Xie, S. Gong and C. Yang, Cascade Chirality Transfer through Diastereomeric Interaction Enables Efficient Circularly Polarized Electroluminescence, *Adv. Funct. Mater.*, 2023, **33**, 2215179.
41 B. H. Drummond, G. C. Hoover, A. J. Gillett, N. Aizawa, W. K. Myers, B. T. McAllister, S. T. E. Jones, Y. Pu, D. Credgington and D. S. Seferos, Selenium Substitution Enhances Reverse Intersystem Crossing in a Delayed Fluorescence Emitter, *J. Phys. Chem. C*, 2020, **124**, 6364–6370.
42 Y. Hu, J. Miao, T. Hua, Z. Huang, Y. Qi, Y. Zou, Y. Qiu, H. Xia, H. Liu, X. Cao and C. Yang, Efficient selenium-integrated TADF OLEDs with reduced roll-off, *Nat. Photonics*, 2022, **16**, 803–810.
43 Y. Zou, M. Yu, Y. Xu, Z. Xiao, X. Song, Y. Hu, Z. Xu, C. Zhong, J. He, X. Cao, K. Li, J. Miao and C. Yang, Acceleration of reverse intersystem crossing in multi-resonance TADF emitter, *Chem*, 2024, **10**, 1485–1501.
44 J. Hu, J. Liang, Z. Yan, H. Ni, X. Liao and Y. Zheng, One-shot synthesis of heavy-atom-modified carbazole-fused multi-resonance thermally activated delayed fluorescence materials, *Sci. China Mater.*, 2024, **67**, 2789–2795.
45 Q. Zheng, Y. Qu, P. Zuo, H. Yuan, Y. Yang, Y. Qiu, L. Liao, D. Zhou and Z. Jiang, Enhancing multi-resonance thermally activated delayed fluorescence emission via through-space heavy-atom effect, *Chem*, 2025, **11**, 102353.
46 H. Ma, Q. Peng, Z. An, W. Huang and Z. Shuai, Efficient and Long-Lived Room-Temperature Organic Phosphorescence: Theoretical Descriptors for Molecular Designs, *J. Am. Chem. Soc.*, 2019, **141**, 1010–1015.
47 C. Chan, M. Tanaka, Y. Lee, Y. Wong, H. Nakanotani, T. Hatakeyama and C. Adachi, Stable pure-blue hyperfluorescence organic light-emitting diodes with high-efficiency and narrow emission, *Nat. Photonics*, 2021, **15**, 203–207.
48 CCDC 2408523: Experimental Crystal Structure Determination, 2025, DOI: **10.5517/ccdc.csd.cc2lv891**.